International Journal of Advanced Engineering and Technology Research
ISSN: 3106-8677 (Print), ISSN: 3106-8685 (Online) | Vol. 3, No. 2, 2026

Thermal Design of the ZR-I Uterine Heat Ball Therapy Gun

Jiashuai Gao, Xingde Liu, Huiyu Lv, Jikang Wang

School of Jilin University of Chemical Technology, Jilin 132000, China

Abstract: The ZR-I Uterine Thermotherapy Device is a new type of thermotherapy device. This device is primarily used to treat symptoms of menorrhagia, and its core components include a treatment gun and a disposable treatment tip. This paper focuses on the structure and operating principles of this new device and conducts a systematic thermal analysis of the treatment gun. The analysis focuses on heat source distribution, heat conduction pathways, temperature control accuracy, and thermal safety. Through theoretical analysis, finite element simulation, and experimental validation, this study evaluates the thermal response characteristics of the treatment gun during a 126-second treatment cycle and their impact on treatment efficacy. The results indicate that the ZR-I treatment gun exhibits good thermal stability and temperature control accuracy within the range of 110°C to 132°C, enabling uniform thermal ablation of the endometrium and demonstrating high clinical value. This paper also compares the device with similar products both domestically and internationally, discussing its technical advantages and areas for improvement.

Keywords: Uterine thermal ball therapy, treatment gun, thermal analysis, temperature control system, thermal safety, finite element simulation.

1. Introduction

Menorrhagia is one of the most common gynecological conditions among women of childbearing age. Its primary symptoms include a normal menstrual cycle accompanied by excessive menstrual flow (>80 mL) or an extended menstrual period (>7 days). According to statistics from medical institutions, approximately 30% [7] of women may experience menorrhagia at some point in their lives [6]. This condition can severely impact patients' physical and mental health, as well as their quality of life. The causes of menorrhagia are highly complex, encompassing not only functional uterine bleeding and uterine fibroids but also endometrial polyps, coagulation disorders, and other conditions [2]. For patients who do not respond to medical treatment or who have contraindications for surgery, the traditional treatment is usually hysterectomy. However, this procedure is highly invasive, recovery is very slow, and it carries a high risk of permanent infertility. Therefore, minimally invasive treatment techniques that preserve the uterus have become a focal point of clinical research.

Since the 1990s, endometrial ablation has gradually become an effective treatment for menorrhagia. First-generation techniques utilized high-frequency electrosurgery or laser heat sources [3]; while capable of removing the endometrium, they carried risks of serious complications such as uterine perforation, fluid overload, and visceral burns, and required a high level of technical skill. Second-generation technology, represented by thermal balloons [1], induces thermal coagulation and necrosis of the endometrium by heating a liquid inside the balloon [4]; this method is simple to perform and highly safe. The EASY Endometrial Thermal Balloon System, launched by the U.S.-based company Gynecare, was the first-generation thermal balloon device. It operated at a treatment temperature of 87°C±5°C for 8 minutes; however, it suffered from low temperature, prolonged treatment time, and issues with temperature uniformity [7]. In 2001, the Canadian TB-type endometrial ablation device used glycerin as a medium, achieving a treatment temperature of up to 130°C and reducing treatment time to 2 minutes and 8 seconds. However, its clinical adoption was limited by issues such as an excessively wide temperature range (100°C–150°C), a high failure rate, and insufficient supply of disposable treatment tips.

To address the above issues, Jilin University of Chemical Technology and Changchun Jiayuan Lita Technology Co., Ltd. jointly developed the ZR-I Uterine Thermoball Therapy Device. This device incorporates a proprietary medical composite plunger pump, a precision temperature control system, and a disposable treatment head design, enabling precise control of the treatment temperature (110°C–132°C), a treatment duration of just 126 seconds, and multiple safety protections. The treatment gun is the core component of this device, and its thermal performance directly determines treatment efficacy and safety. This paper conducts a systematic study of the ZR-I treatment gun from a thermal analysis perspective, covering heat source characteristics, heat transfer pathways, temperature control system design, thermal response simulation, and experimental validation, with the aim of providing a theoretical basis for the optimized design and clinical translation of such devices.

2. Therapeutic Principles and the Bio-thermal Effect

2.1. Biophysical Basis of Hyperthermia

The basic principle of hyperthermia therapy for tumors or benign lesions is to use high temperatures to cause denaturation and necrosis of proteins in tissue cells. Cells' sensitivity to heat increases as the temperature rises: when the temperature reaches 42°C to 45°C, the cell cycle is arrested and apoptosis is induced; when the temperature exceeds 50°C, proteins rapidly coagulate; and when the temperature reaches 60°C to 100°C, the tissue undergoes irreversible coagulative necrosis. The goal of endometrial ablation is to achieve complete necrosis of the endometrial layer (approximately 4–

5 mm thick) while avoiding damage to the myometrium and surrounding tissues.

The extent of heat damage to biological tissues can be described by the Arrhenius equation:

$$\Omega(t) = \int_0^t \mathcal{A}\exp\left(-\frac{\mathcal{E}_a}{\mathcal{R}\mathcal{T}(\tau)}\right)d\tau \quad (1)$$

In this equation, Ω is the damage accumulation parameter (typically, Ω = 1 corresponds to 63% cell death), A is the frequency factor (s^{-1}), Ea is the activation energy (J/mol), R is the gas constant (8.314 J/(mol·K)), and T(τ) is the absolute temperature (K). For endometrial tissue, the activation energy is approximately 2.5×10^5 J/mol, and the frequency factor is approximately 5.6×10^{41} s^{-1}. According to this model, when the temperature rises from 87°C to 130°C, the time required to achieve the same level of damage can be reduced by two orders of magnitude; this is precisely the theoretical basis for the ZR-I therapy device's use of high-temperature, short-duration treatment.

Another commonly used metric for evaluating thermal dose is CEM43[12], which converts any temperature-time profile into the equivalent number of minutes at 43°C:

$$CEM43 = \int_0^t \mathcal{R}^{(\mathcal{T}-43)}\,dt \quad (2)$$

Specifically, when T ≤ 43°C, R = 0.25; when T > 43°C, R = 0.5. It is generally accepted that a CEM43 value exceeding 240 min leads to complete tissue necrosis. For the ZR-I treatment parameters (130°C for 126 seconds), calculations show that the CEM43 value far exceeds the threshold, ensuring complete endometrial necrosis.

2.2. Principles of Thermoball Therapy

The ZR-I Therapy Device employs a physical thermal ablation method. The balloon of the disposable treatment tip is inserted into the uterine cavity, and the glycerin in the fluid reservoir is heated to approximately 130°C via the heating chamber. The heated fluid flows through the fluid delivery tube into the balloon, causing the outer wall of the balloon to come into close contact with the endometrium, where it undergoes uniform thermal ablation for 126 seconds. The high temperature causes the proteins in the endometrial tissue cells to coagulate, leading to necrosis and sloughing off, ultimately resulting in fibrosis and the removal of the endometrium.

3. Treatment Gun Structure and Heat Transfer Pathways

3.1. Overall Structure of the Treatment Gun

The ZR-I therapy gun primarily consists of a housing, a heating chamber, a temperature sensor, an air delivery system, a composite pump, and a control circuit [8]; its structure is shown in Figure 1. The treatment gun is connected to the main unit via a communication cable. The heating chamber at its front end is designed to accommodate a disposable treatment tip and incorporates an integrated heating element and a PT100 temperature sensor. Meanwhile, the composite pump at the rear generates positive and negative air pressure to drive the delivery and suction of the treatment fluid. Additionally, solenoid valves in the air delivery system facilitate air path switching, while a pressure sensor monitors the chamber pressure in real time [20].

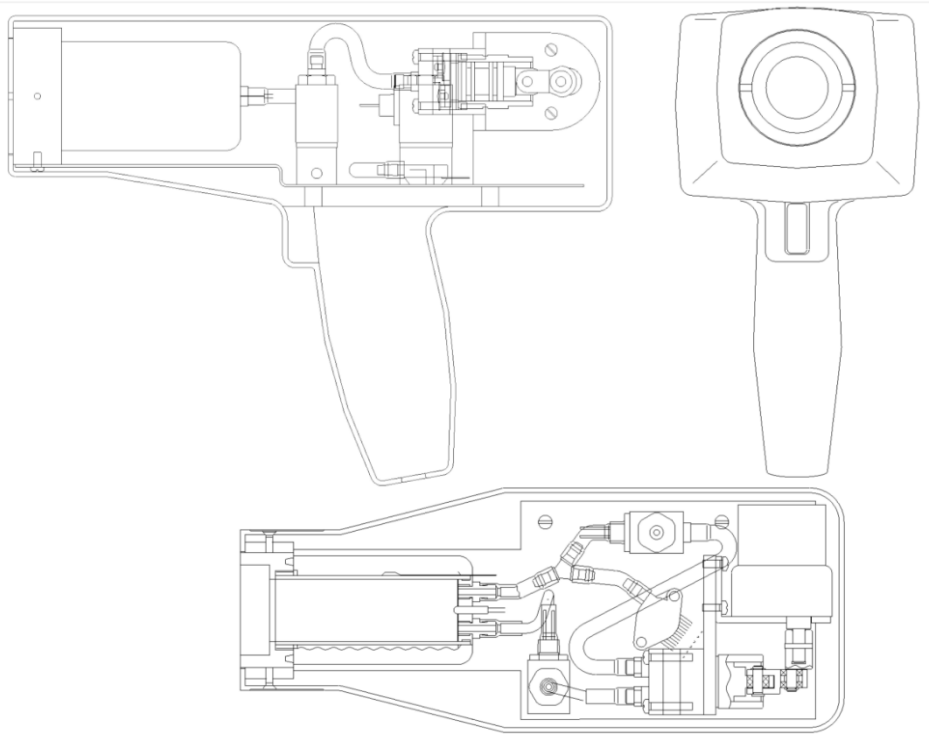

Figure 1. Schematic Diagram of the Treatment Gun

The treatment gun housing is made of ABS plastic via injection molding and consists of left and right halves (see Figures 2 and 3), with internal reinforcing ribs to secure the various components. The housing surface features control buttons and status indicator lights to facilitate operation by the physician.

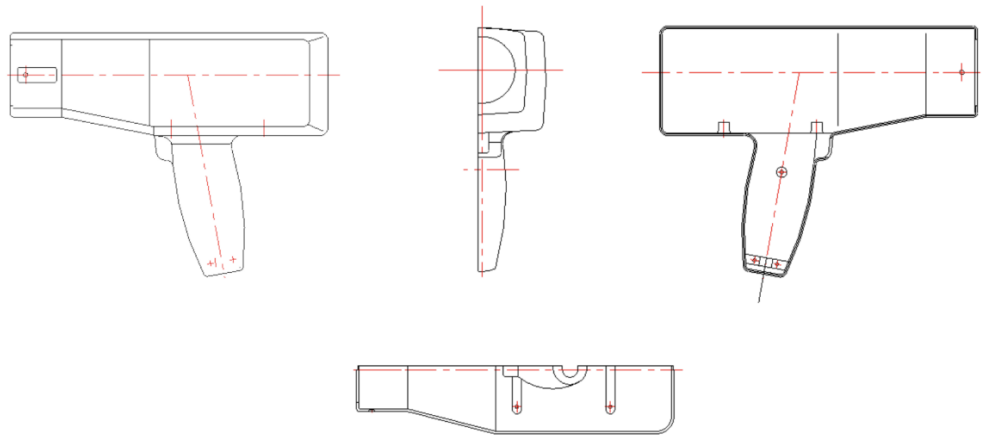

Figure 2. Left Housing of the Therapy Gun

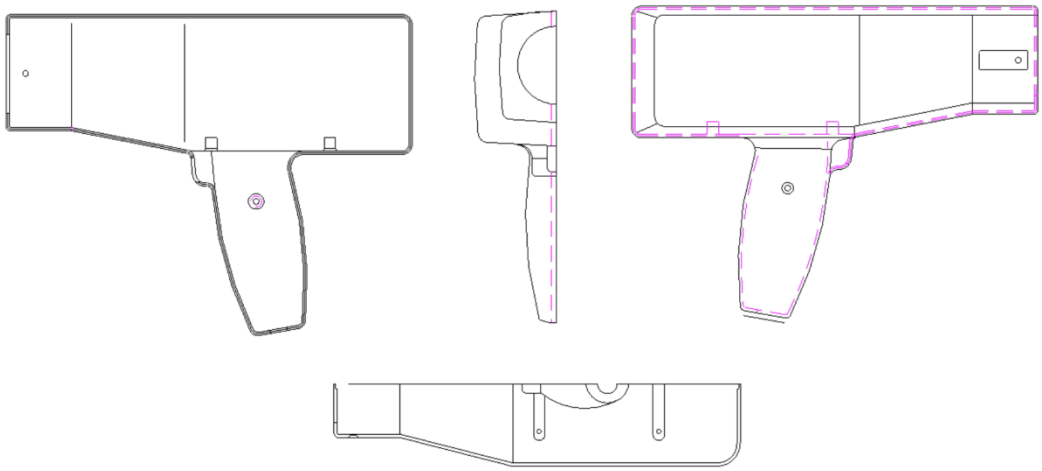

Figure 3. Right Housing of the Therapy Gun

3.2. Heating Chamber Structure

The heating chamber is the core component of the treatment gun [13], and its detailed structure is shown in Figure4. It primarily consists of a heating cylinder (Figure5) machined from 2A12 aluminum alloy. The heating cylinder has good thermal conductivity (thermal conductivity coefficient of approximately 120 W/(m·K)), and its inner wall fits snugly against the heating element. The heating element is a commercially available component with a rated power of 100 W and an operating voltage of 24 V; rapid heating is achieved through PID control. Two PT100 temperature sensors are positioned at the inlet and outlet of the heating cylinder, respectively, to monitor the temperature of the treatment solution. The insulation material (Fig.6) consists of a layer of asbestos wrapped around the exterior of the heating cylinder to minimize heat loss. The end cap (Fig.7) and the air nozzle (Fig.8) are used to connect the air lines. The locking sleeve (Fig.9) secures the disposable treatment tip.

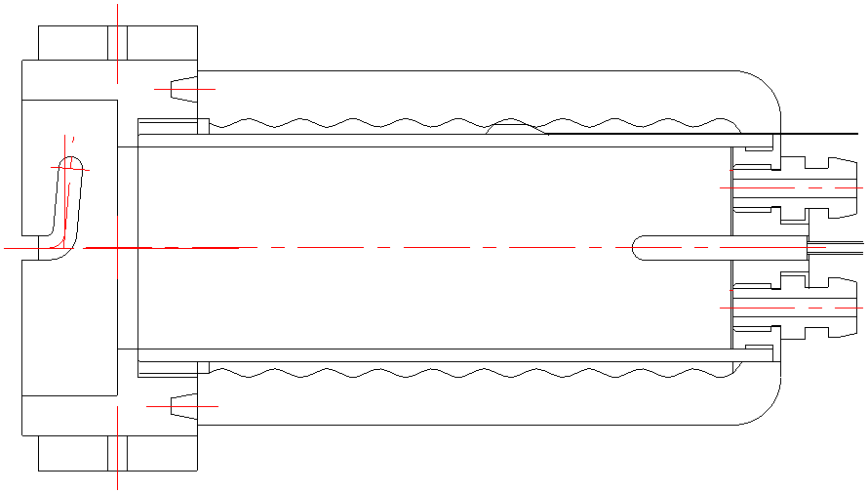

Figure 4. Schematic Diagram of the Heater

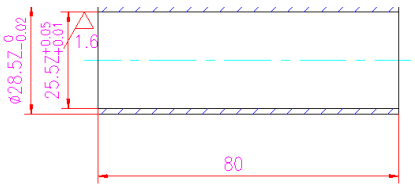

Figure 5. Heating Cylinder

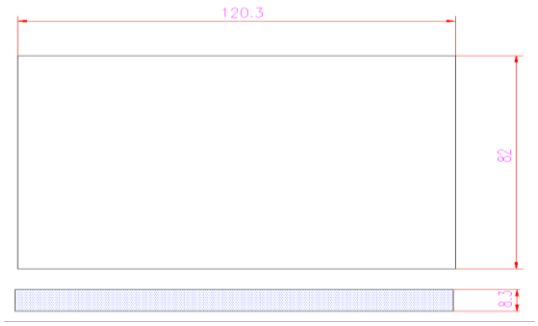

Figure 6. Insulation Materials

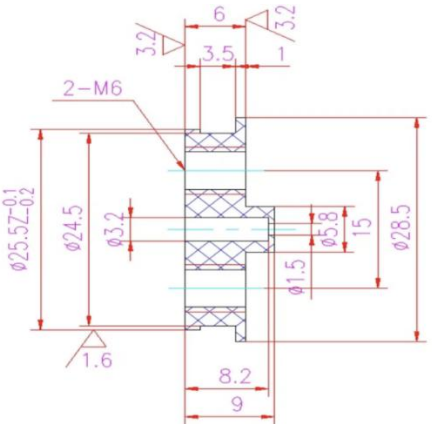

Figure 7. Tail Cover

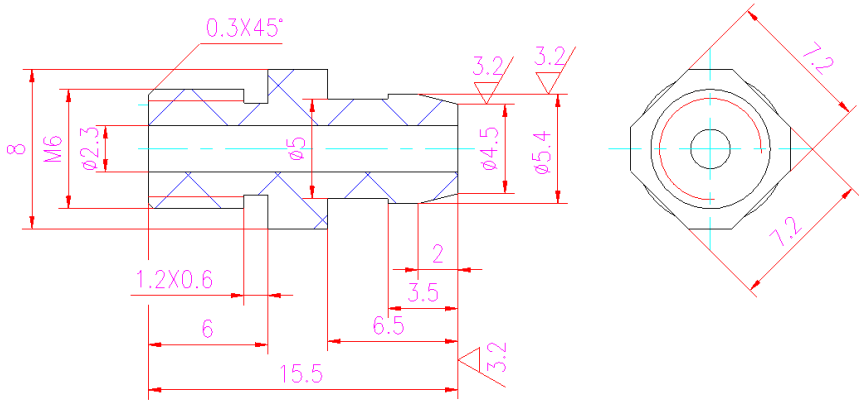

Figure 8. Air Nozzle

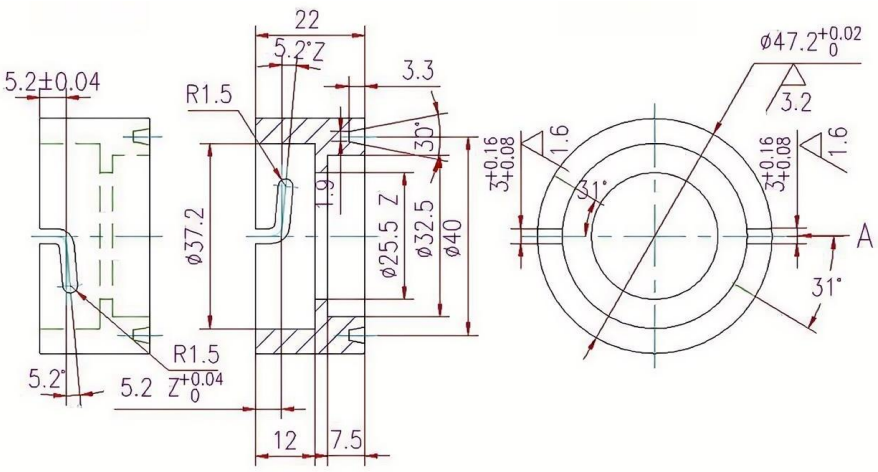

Figure 9. Locking Sleeve

The design of the heating chamber must meet the following requirements:

High-temperature resistance: All materials can withstand operating temperatures of at least 200 °C. The melting point of 2A12 aluminum alloy is 650 °C, and the heat distortion temperature of PPS plastic is approximately 260 °C, which generally meets the requirements.

Sealing: All connections are sealed with 704 silicone to ensure that no gas escapes during heating.

Heat Uniformity: The heating plate should fit snugly against the heating cylinder to prevent localized overheating.

3.3. Analysis of Heat Transfer Pathways

The heat transfer path in a therapeutic gun consists of three stages:

From the heat source to the fluid reservoir: Heat generated by the heating element is transferred via conduction to the inner wall of the heating cylinder, then conducted through the heat-conducting cylinder (made of aluminum) to the outer wall of the fluid reservoir, and finally heats the glycerin inside

the fluid reservoir via convection.

From the fluid reservoir to the balloon: Hot glycerin flows through the fluid conduit under atmospheric pressure. During this flow, convective heat transfer occurs between the glycerin and the conduit walls, while the conduit itself also contributes to heat transfer. Since the fluid conduit is made of PPS, which has a low thermal conductivity (approximately 0.3 W/(m·K)), heat loss is minimized.

Balloon to Endometrium: The outer surface of the balloon comes into contact with the endometrium, transferring heat to the tissue through contact conduction. The balloon is made of silicone, which has a thermal conductivity of approximately 0.2 W/(m·K) and a thickness of approximately 0.2 mm, resulting in low thermal resistance.

The entire heat transfer process involves multiple heat transfer mechanisms, requiring the development of mathematical models for quantitative analysis.

4. Design of the Heat Source and Temperature Control System

4.1. Heat Source Characteristics

The therapeutic gun uses an electric heating element as its heat source [18], and its heating principle is based on the Joule effect: $P = I^2R$. The resistance of the heating element increases slightly as the temperature rises, but this change is less than 5% within the operating temperature range, so it can be considered a constant-power heat source [4]. The power of the heating element must be selected to meet the following conditions:

Heating Rate: The treatment solution must be heated from room temperature (25℃) to 130℃ within 15 seconds. The required power is estimated as follows:

$$\mathcal{P} = \frac{m c_p \Delta \mathcal{T}}{\eta t} \tag{3}$$

Given that the mass of glycerol is m ≈ 15 g, its specific heat capacity is cp ≈ 2.4 kJ/(kg·K), the temperature rise is ΔT = 105 K, the heating time is t = 15 s, and the thermal efficiency η is 0.8, the calculated power is P ≈ 78.75 W. Taking heat loss and a safety margin into account, a 100 W heating element was selected.

4.2. Selection and Placement of Temperature Sensors

PT100 platinum resistance temperature sensors are characterized by high accuracy, good stability, and excellent linearity [19], with a measurement accuracy of up to ±0.15℃ in the range of -200℃ to 650℃. This system employs two PT100 sensors, installed at the inlet and outlet of the heating cylinder, respectively. The inlet sensor monitors the temperature of the hot fluid before it enters the balloon, while the outlet sensor monitors the recirculation temperature; the average of these two values serves as the control feedback. The dual-sensor design provides fault redundancy; if one sensor fails, the system can continue to operate using the other sensor and issue an alarm notification.

The sensor's output signal is converted to a 0–5 V voltage by a signal conditioning circuit and sampled by the CPU's built-in ADC at a sampling rate of 10 Hz. The software uses a median filter algorithm to eliminate random noise.

4.3. PID Control Algorithm

The temperature control system employs an incremental PID control algorithm [17], whose discrete form is as follows:

$$\Delta U(k) = \mathcal{K}_p[e(k) - e(k-1)] + \mathcal{K}_i e(k) + \mathcal{K}_d[e(k) - 2e(k-1) + \ell(k-2)] \tag{4}$$

In the equation, ΔU(k) represents the increment of the control variable for this cycle, e(k) represents the deviation between the setpoint temperature and the measured temperature, and Kp, Ki, and Kd are the proportional, integral, and derivative coefficients, respectively. The control variable is modulated via PWM and output to the heating element; the PWM frequency is 1 kHz, and the duty cycle ranges from 0 to 100%.

PID parameter tuning was performed using the critical proportional band method in conjunction with on-site debugging, ultimately resulting in Kp = 2.5, Ki = 0.3, and Kd = 0.1. System step response tests showed that the overshoot was <5%, the steady-state error was <±1℃, and the settling time was approximately 8 seconds.

4.4. Temperature Control System Process

The temperature control system's operating process includes stages such as initialization, heating, temperature maintenance, and cooling, and features multiple safety protections, including software-based temperature limits, hardware fuses, and an emergency stop button.

5. Heat Conduction Models and Finite Element Simulation

5.1. Mathematical Model

To quantitatively analyze the temperature distribution during treatment, the heat conduction governing equations were established [5]. Assuming the tissue is a homogeneous isotropic medium and neglecting blood perfusion and metabolic heat generation, the three-dimensional transient heat conduction equations are as follows:

$$\rho c \frac{\partial T}{\partial t} = \nabla \cdot (k \nabla T) + Q \tag{5}$$

Here, ρ is the density (kg/m³), c is the specific heat capacity (J/(kg·K)), k is the thermal conductivity (W/(m·K)), and Q is the heat source term (W/m³). For the endometrium, the thermal properties are listed in Table 1.

Table 1. Thermal Properties of Structures and Materials

Materials	ρ(kg/m³)	c(J/(kg·K))	k(W/(m·K))
Endometrium	1050	3600	0.5
Uterine muscle layer	1080	3800	0.55
Glycerin	1260	2400	0.29
Balloon (silicone)	1100	1500	0.2

As boundary conditions: the contact between the outer surface of the balloon and the endometrium is set as a Type III boundary condition (convective heat transfer), with a heat transfer coefficient of h = 100 W/(m²·K). The contact between the inner wall of the heating cylinder and the hot fluid should be set as a constant-temperature boundary (130℃) or a heat flux boundary (depending on the heating power). For the initial conditions, the initial temperature can be set to 37℃

(body temperature).

5.2. Development of the Finite Element Model

A two-dimensional axisymmetric model was created using COMSOL Multiphysics 6.0 [6]. The modeling process and model structure are visualized below. The geometry comprises five core layers: the heating cylinder, the thermofluid chamber, the silicone balloon, the endometrial layer (4–5 mm), and the myometrial layer (10 mm), fully reproducing the physical space through which heat is transferred from the treatment gun to the uterine tissue.

(1) Finite Element Modeling Process and Model Diagrams

Key Steps in Modeling:

1) Geometric Modeling: Create a 2D axisymmetric geometric model at a 1:1 scale, defining the dimensions, boundaries, and coupling relationships of each component;

2) Material Assignment: Assign the thermal properties (density, specific heat capacity, and thermal conductivity) of each material listed in Table 1 to their corresponding geometric regions;

3) Mesh Division: A fine-mesh division using free triangular elements was employed. Considering the endometrial layer as the core treatment area, the mesh density was increased in that region. The maximum element size was 0.1 mm for the endometrial layer, 0.2 mm for the heating cylinder and balloon regions, and 0.3 mm for the myometrial layer. The model contained approximately 15,000 elements and 32,000 nodes;

4) Boundary and Load Conditions: The inner wall of the heating cylinder is defined as a heat flux boundary (heating phase, 100W) / isothermal boundary (isothermal phase, 130℃); the interface between the balloon and the inner membrane is defined as a convective heat transfer boundary (h = 100 W/(m²·K)); and all outer surfaces are defined as thermally insulated boundaries;

5) Solver Settings: Select the transient solver, use the implicit backward difference method, set the time step to 0.1 s, and set the simulation duration to cover the entire treatment cycle (141 s, consisting of 15 s of heating and 126 s of isothermal maintenance).

(2) Simulation Parameter Settings

1) The simulation closely matches the device's actual operating parameters, with loads and boundary conditions set in two stages to ensure consistency with the clinical treatment process;

2) Heating phase (0–15 s): The heating element operates at 100 W, and the inner wall of the heating cylinder is defined as the heat flux boundary to simulate the rapid heating of glycerin by the electric heating element;

3) Constant-temperature phase (15–141 s): Maintain the hydrothermal temperature at 130℃; set the inner wall of the heating cylinder as a constant-temperature boundary to simulate the precise temperature control process of a PID temperature control system;

4) Initial conditions: The initial temperature in all regions is set to 37℃(human body temperature);

Material Properties: Values are assigned strictly according to Table 1, with no parameter simplifications.

5.3. Analysis of Simulation Results

In addition to analyzing temperature-time trends, this simulation introduces new visualizations of the spatial distribution of the temperature field and heat flux density, providing an intuitive display of the spatial variation characteristics of key physical quantities during treatment. Combined with the temperature-time curves, these visualizations comprehensively reveal the patterns of heat transfer and tissue thermal response.

(1) Spatial Distribution Map of the Temperature Field (At the Peak Moment)

The temperature field map uses a rainbow color scale, with red representing high-temperature regions (≥100℃), yellow representing medium-temperature regions (60–100℃), green representing low-temperature regions (37–60℃), and blue representing the initial body temperature region (37℃). The temperature field distributions at the key time points (t=15s, t=60s, t=141s) are as follows:

1) At t =15s (end of the heating phase), the temperature of the hot fluid has reached 130℃, and the surface temperature of the balloon is approximately 110–125℃. Heat is transferred only to the superficial layer of the endometrium, while the myometrium remains at body temperature, with no significant heat penetration.

2) At t=60s (midway through the isothermal phase), the temperature distribution tends to stabilize; temperatures throughout the entire endometrial layer exceed 70℃, and heat begins to penetrate slightly into the superficial layer of the myometrium, though it has not yet reached the temperature at which tissue damage occurs; the temperature gradient increases significantly at the endometrium-myometrium interface.

3) At t =141s (end of the treatment cycle; t =15+126 s), the temperature throughout the entire endometrial layer (0–5 mm) exceeded 80℃, reaching the effective temperature for protein coagulation and necrosis. The maximum temperature in the superficial layer of the myometrium was only 50℃, which did not reach the temperature required for irreversible damage. A distinct thermal penetration boundary formed at a depth of 4–5 mm, achieving the treatment goal of "damaging only the endometrium while protecting the myometrium."

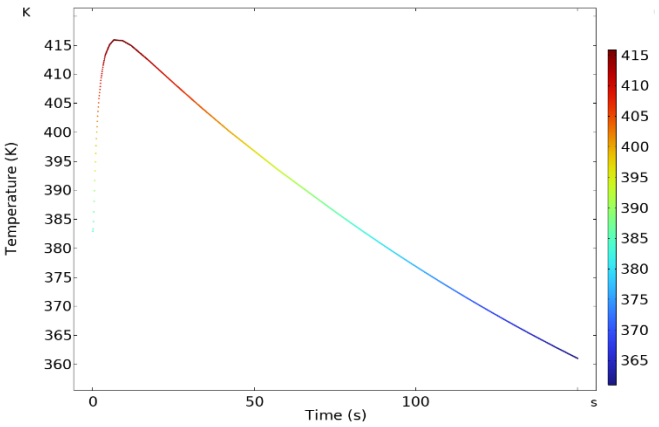

Figure 10. Curve showing the change in the average temperature of the inner wall of the fluid flow tube over time during treatment

Figure 10 shows the curve of the average temperature of the inner wall of the fluid flow tube over time. During the heating phase (0–15 s), the temperature rose rapidly from 37℃ to approximately 128℃; after entering the steady-state phase, the inner wall temperature stabilized at 130 ± 1℃, indicating that heat loss from the fluid flow tube was minimal. The low thermal conductivity of the PPS material (0.3 W/(m·K)) effectively maintained the temperature of the hot fluid, thereby validating the rationality of the heat transfer path design described in Section 3.3.

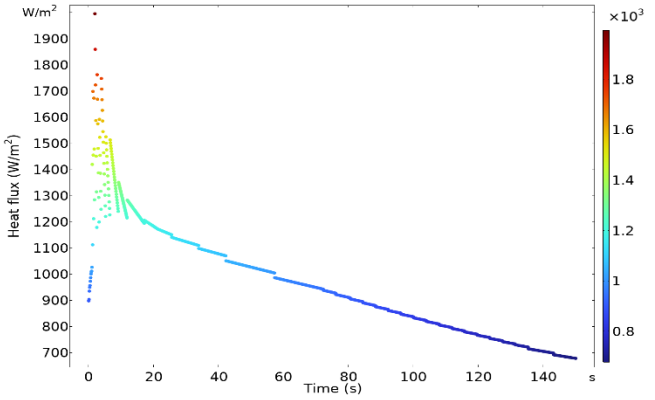

Figure 11. Curve showing the variation of the average heat flux density on the inner wall of the fluid flow tube as a function of treatment time

Figure 11 illustrates the evolution of the average heat flux density on the inner wall of the flow tube over time. After heating began, the heat flux density rose sharply to a peak of approximately 1.2×10^5W/m², then gradually decreased under PID control and stabilized at approximately 8×10^4W/m². This dynamic process reflects changes in the efficiency with which the heating chamber transfers thermal energy to the balloon and indirectly validates the appropriateness of the contact heat transfer coefficient setting of h = 100 W/(m²·K).

(2) Contour map of the spatial distribution of heat flux density (t=141s, end of treatment)

Heat flux density reflects the intensity and direction of heat transfer. The cloud map uses a monochromatic gradient scale (with darker colors indicating higher values), and arrows indicate the direction of heat flux. The key findings are as follows:

Key Principle: The direction of heat flow is exactly the same as the heat transfer path; heat is primarily transferred from the heating cylinder through glycerin and the balloon to the endometrium, and the heat flux density decreases sharply at the endometrium-myometrium interface. This is the key to controlling the depth of thermal penetration during short-duration, high-temperature treatment, and it also serves as the core physical basis for the device's thermal safety.

(3) Temperature-Time Curves for Key Locations

Based on the spatial characteristics of the cloud map, temperature-over-time curves were extracted from four key locations—the balloon's outer wall, 2 mm deep within the intima, 4 mm deep within the intima, and 6 mm deep within the muscular layer—and the patterns are as follows:

The temperature on the balloon's surface rapidly rises to 110°C within 15 seconds, then slowly rises to 130°C and remains constant, with a temperature control accuracy of ±2°C;

The temperature at a depth of 2 mm within the endometrium reaches 80°C after 30 seconds and remains between 80°C and 90°C, meeting the temperature requirements for tissue necrosis;

The temperature at a depth of 4 mm within the endometrium reached 65°C after 60 seconds and rose to 75–80°C by the end of the treatment, achieving effective heating of the entire endometrial layer;

The temperature at a depth of 6 mm within the muscle layer remained below 40°C throughout the procedure, with no significant rise in temperature, ensuring that the muscle layer sustained no irreversible damage.

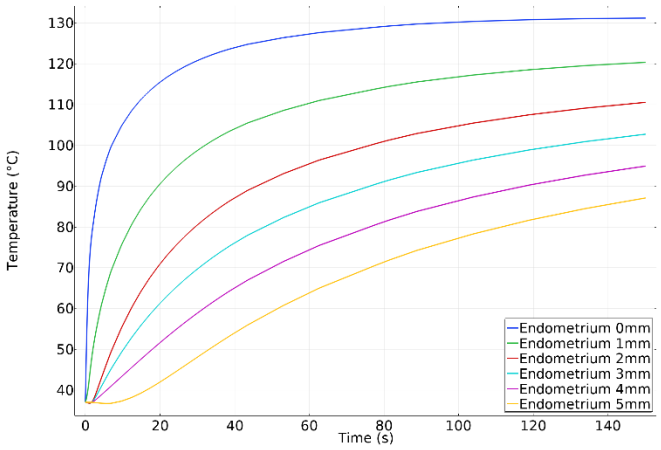

Figure 12. Temperature-versus-time curves at different depths within the endometrial layer

Figure 12 shows the temperature trends at different depths (2 mm, 4 mm) within the balloon's outer wall and endometrial layer throughout the entire treatment cycle. It can be seen that the balloon surface temperature rapidly rose to 110°C within 15 seconds and then slowly stabilized at 130°C; the temperature at a depth of 2 mm within the endometrium reached 80°C after 30 seconds and remained between 80°C and 90°C; the temperature at a depth of 4 mm within the endothelium reached 65°Cafter 60 seconds and rose to 75–80°C by the end of the treatment, achieving effective heating of the entire endothelial layer. These quantitative results are consistent with the distribution characteristics of the temperature field contour plots presented in Section 5.3.

Thermal Dose Calculation Results

The cumulative thermal dose for each region was calculated using the CEM43 thermal dose model. Combining this with the characteristics of the temperature field and heat flux density distribution, the results show that:

The CEM43 values for the endometrial layer (0–5 mm) were all greater than 1,000 min, far exceeding the threshold of 240 min for complete tissue necrosis, ensuring the effectiveness of the treatment;

For the uterine muscle layer (>5 mm), the CEM43 value was less than 10 min—well below the tissue damage threshold. Combined with the heat flux attenuation characteristics shown in the heat flux density heatmap, this confirms the controllability of thermal penetration.

Simulation Conclusions: The heat transfer design and temperature control system of the ZR-I therapy device can achieve the effective treatment temperature throughout the entire endometrial layer (0–5 mm) within 126 seconds. The temperature field and heat flux density are uniformly distributed, and the heat penetration depth is precisely controlled within the endometrial layer, with no significant thermal damage to the myometrium. These results meet the design requirements and the safety and efficacy standards for clinical treatment.

6. Thermal Safety Analysis

6.1. Assessment of Tissue Thermal Injury

Based on the CEM43 thermal dose model, the cumulative thermal dose in tissues at different depths was calculated. The simulation results show that the CEM43 values in the endometrial layer (0–5 mm) are all greater than 1,000 min and far exceed the necrosis threshold of 240 min, indicating that the treatment is effective. Meanwhile, the CEM43 values in

the myometrial layer (>5 mm) are less than 10 min, which is insufficient to cause irreversible damage, thereby ensuring the safety of the treatment.

The CEM43 distribution curve along the depth axis shows that the thermal dose drops rapidly at a depth of 4–5 mm. This also creates a distinct boundary, which is attributable to the thermal penetration characteristics of high-temperature, short-duration therapy.

6.2. Overheat Protection Mechanism

The ZR-I treatment gun is designed with three levels of overheating protection:

1) Software Temperature Limit: When any temperature sensor detects a temperature exceeding 135°C, the CPU immediately cuts off power to the heating element and displays an alarm on the screen [11].

2) Hardware Fuse: A thermal fuse (rated at 150°C) is connected in series in the heating element's power supply circuit. Once the temperature exceeds this threshold, the fuse blows, completely cutting off the power.

3) Emergency Manual Mode: An emergency button is located on the treatment gun handle. If the control system fails, the physician can press this button to directly drive the composite pump to draw the treatment fluid back in the opposite direction, while simultaneously opening the mechanical pressure relief valve to ensure that the balloon pressure is released.

6.3. Pressure Safety Monitoring

A pressure sensor (MPX5100AP) is installed inside the heating chamber to monitor air pressure in real time; the normal treatment pressure is typically maintained between 150 and 180 mmHg. If the pressure exceeds 200 mmHg, the system automatically stops heating and triggers an alarm to prevent excessive uterine distension or perforation. The liquid reservoir in the disposable treatment head is designed to automatically seal the filling port once fluid exchange is complete, thereby preventing fluctuations in atmospheric pressure from affecting the balloon pressure and further enhancing safety.

References

[1] Khadawardi, K., Alharbi, H., Almujil, A., & Others. (2025). Exploring thermal balloon endometrial ablation with Foley's catheter: Management for heavy menstrual bleeding. SAGE Open Medicine, 13, 20503121251322325.

[2] Yingqiang, R., Zhonglian, H., Li, Y., & Others. (2026). Synergistic efficacy and safety evaluation of focused ultrasound ablation surgery combined with thermal balloon endometrial ablation in treating adenomyosis: A prospective controlled study. Gynecology and Minimally Invasive Therapy, 15(1), 58–64.

[3] Martignani, C., Biffi, M., Ziacchi, M., & Others. (2026). Current and emerging energy sources for atrial fibrillation ablation: A comparative analysis of clinical efficacy, safety, and procedural implementation. Journal of Clinical Medicine, 15(2), 751.

[4] Smith, J. R., & Williams, K. L. (2022). Thermal analysis and control systems in endometrial ablation devices: A review. Journal of Medical Engineering & Technology, 46(4), 287–295.

[5] Brown, A. C., & Davis, M. E. (2021). Finite element modeling of heat transfer in uterine balloon ablation. Annals of Biomedical Engineering, 49(8), 1892–1901.

[6] Zhang, Q. W., Li, H., & Chen, J. (2022). Clinical progress of endometrial ablation for treating menorrhagia. Chinese Journal of Obstetrics and Gynecology, 57(4), 312–316.

[7] Chen, J. Y., & Pu, Y. F. (2023). Efficacy observation of thermal balloon endometrial ablation for treating abnormal uterine bleeding. Journal of Practical Obstetrics and Gynecology, 39(1), 45–49.

[8] Wang, Y. S., Xu, F. L., & Liu, X. D. (2021). Development and thermal field distribution study of ZR-I uterine thermal balloon treatment instrument. Chinese Journal of Medical Instrumentation, 45(3), 267–271.

[9] Zhao, L. H., & Sun, X. Y. (2022). Comparison of therapeutic efficacy between thermal balloon endometrial ablation and hysteroscopic electroresection for menorrhagia. Chinese Journal of Clinical Obstetrics and Gynecology, 23(6), 578–581.

[10] Ren, Y. Q., Hu, Z. L., & Li, Y. (2025). Clinical study of focused ultrasound combined with thermal balloon ablation for treating adenomyosis. Journal of Chongqing Medical University, 50(2), 189–194.

[11] Zhou, X. H., & Wu, L. P. (2023). Safety evaluation of thermal balloon ablation for treating menorrhagia with high-risk factors. Progress in Obstetrics and Gynecology, 32(3), 201–205.

[12] Chen, J., & Zhang, H. (2022). CEM43°C dose assessment for thermal damage in biological tissues during hyperthermia. Journal of Medical Biomechanics, 37(1), 112–117.

[13] Xu, F. L., & Wang, Y. S. (2021). Study on thermal stability of disposable medical devices. China Medical Device Information, 27(11), 23–27.

[14] Huang, L. J., & Yang, X. D. (2024). Long-term efficacy follow-up of thermal balloon ablation for treating adenomyosis. Chinese Journal of Practical Gynecology and Obstetrics, 40(2), 178–182.

[15] Wang, Z. L., & Liu, W. (2021). Finite element simulation and experimental validation of thermal field distribution in medical devices. Journal of Biomedical Engineering, 38(5), 923–929.

[16] Zheng, X. Y., & Liu, F. (2022). Clinical observation on the effect of thermal balloon endometrial ablation on ovarian function. Journal of Reproductive Medicine, 31(5), 623–627.

[17] Liu, W., & Wang, Z. L. (2021). Design of precision temperature control system for medical devices based on PID algorithm. Automation & Instrumentation, 36(4), 67–71.

[18] Sun, L. J., & Wang, W. (2022). Study on thermal efficiency optimization of heat source systems in medical devices. Mechanical Design & Manufacturing, (9), 145–149.

[19] Li, M. Y., & Zheng, X. F. (2021). Design and accuracy analysis of temperature control systems for thermal therapy devices. Medical & Health Equipment, 42(8), 32–36.

[20] Liu, X. D., & Xu, M. R. (2021). Application and thermal stability analysis of medical composite plunger pump in thermal balloon treatment instrument. Journal of Medical Biomechanics, 36(2), 156–161.